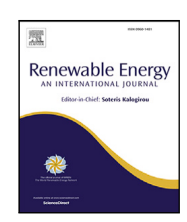
ELSEVIER

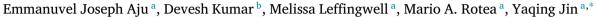
Contents lists available at ScienceDirect

Renewable Energy

journal homepage: www.elsevier.com/locate/renene



The influence of yaw misalignment on turbine power output fluctuations and unsteady aerodynamic loads within wind farms



^a Center for Wind Energy and Department of Mechanical Engineering, The University of Texas at Dallas, Richardson, TX, 75080, United States of America ^b Center for Wind Energy and Department of Electrical and Computer Engineering, The University of Texas at Dallas, Richardson, TX, 75080, United States of America

ARTICLE INFO

Keywords: Wind farm Yaw misalignment Power output fluctuations Unsteady aerodynamic loads

ABSTRACT

Systematic wind tunnel experiments were performed to quantify the power output fluctuations and unsteady aerodynamic loads of modeled wind farms with 3 rows and 3 columns across various yaw angles. Time-resolved particle image velocimetry (PIV) was applied to characterize the flow statistics, while the power output and aerodynamic loads on the turbine tower were measured by a data logger and force cell at high temporal resolution. Results showed that the growth of the yaw misalignment angle mitigates the turbine power output fluctuation. However, this can increase the power fluctuations of downstream turbines. Measurements of the aerodynamic loads on the turbine tower revealed that the growth of the yaw angle significantly increased the fatigue loading in the side-force direction across all frequency components. At the same time, such impact was less distinctive for the thrust force. The dominating unsteady aerodynamic loads are always in the direction perpendicular to the rotor surface. Flow statistics demonstrated that yaw misalignment could effectively increase mean wake velocity, and integral time scale and reduce the turbulence intensity. Finally, theoretical models based on the coupling between turbine properties and local incoming flow statistics were derived to reveal the evolution of turbine power fluctuations and unsteady aerodynamic loads in the wake flow across various yaw misalignment.

1. Introduction

Wind energy has been, and continues to be, an expanding renewable energy source in the United States of America, which has multiplied its installed capacity more than six times during the last decade [1]. The power output of individual turbines within a wind farm is highly influenced by the velocity deficit induced by their upstream counterparts, where a downstream turbine in the wake produces 40% to 60% less power compared to the upstream counterpart with stream-wise spacing of 5 to 7 times rotor diameters between two turbines. [2–4].

Wake steering has proven to be effective in increasing the power output of a wind farm. Wake steering can be achieved by the yaw misalignment between incoming flow and upstream turbines, which induces reduced power output on these units but higher rotor effective wind speeds for the downstream turbines. Early experimental investigations on horizontal axis wind turbine wakes and the visualization of wake deflection associated with yaw misalignment were done by Grant et al. [5] and Grant and Parking [6]. They compared the wake deflection of turbines with two and three blades under yaw misalignment and showed that the wake skew angle for the three-bladed turbine

is higher than the two-blade counterpart. Medici and Alfredsson [7], Fleming et al. [8] and Jimenez et al. [9] illustrated that yaw misalignment can effectively increase the wake flow velocities. Several theoretical, numerical, and experimental studies have been conducted in the last few years to describe the influence of yaw misalignment on wake development and turbine performance, including: (i) wake stream-wise velocity deficit exhibits a kidney-shaped cross-section due to the effect of counter-rotating vortex pair (CVP) [10-15]. (ii) Ground interactions with the CVP causes the yawed turbine wakes to displace either in the positive or negative vertical directions depending on the yaw orientation.[10,15] (iii) The growth of the yaw angle gradually deflects the wake flow and produces an asymmetric velocity deficit about the rotor center-line. [10] (iv) Yaw misalignment alters both coefficients of power (C_n) [16,17] and thrust (C_T) [16,18]. Recently, Bartl et al. [19] experimentally investigated the effect of incoming turbulence and shear on the wake of a yawed turbine and confirmed the above-mentioned phenomena. Computationally inexpensive, simple analytical models can be used to evaluate the effectiveness of yaw control for wake velocity distributions. Shapiro et al. [14] modeled yawed

^{*} Corresponding author.

E-mail address: yaqing.jin@utdallas.edu (Y. Jin).

turbine wake by assuming the rotor as a lifting surface. Bastankah and Porté-Agel [10] utilized experimental data to decompose Reynolds-averaged Navier–Stokes equations, based on which they developed a realistic analytical model to predict both span-wise and stream-wise wake velocities.

Inspired by the effectiveness of yaw misalignment for modulating the wake flow as mentioned above, recent efforts have focused on applying yaw misalignment to increase the power output across wind farms. Howland et al. [20] conducted field tests in Alberta, Canada. They found that wake steering decreased the intermittent power generation and the standard deviation of the wind farm power generation reduced to a maximum of 72%. Campagnalo et al. [21] experimentally investigated the impact of yaw misalignment on three turbines in a wind tunnel. They found that yawing the front row by 20° and the second row by 16° improved the total farm power production by 15%. A very recent study by Zong and Portè-Agel [22] experimentally investigated the effect of yaw misalignment on 3 turbines separated by five times rotor diameters in a single column. They showed that a maximum power improvement of 5.4% was achieved when turbines in the first and second rows are vawed in the same direction. Gebraad et al. [23] developed a parametric model for predicting the power production of wind farms with vaw misaligned turbines. The model was named Flow Redirection and Induction in steady state (FLORIS), This model incorporates the effect of yaw misalignment on the deflection of the turbine wake and also the wind speed deficit in the wake. Schreiber et al. [24] utilized a SCADA (Supervisory control and data acquisition) data collected for 12 months from Wind-park in Dornum, Germany and generated a model with the help of FLORIS. They demonstrated that at low wind speeds optimizing the yaw angles could increase the power output by a maximum of 17%. In addition to experiments and modeling, Gebraad et al. [25] applied computational fluid dynamics to study the effect of yaw misalignment on power production of two aligned NREL 5 MW turbines via Large Eddy Simulation (LES). They illustrated that when the front turbine was yawed from 0° to 40° , the power increment in the second row was more than the power loss in the first row, and the maximum power increase occurred when the front turbine yawed at 25°. Additional work by the same group [26] reported that applying yaw misalignment may simultaneously increase power generation and reduce aerodynamic loads with optimized yaw angles. Waipao et al. [27] utilized Reynolds-averaged Navier-Stokes equations (RANS) to simulate the impact of yaw misalignment on two inline National Renewable Energy Laboratory (NREL) 5 MW turbines. By applying vaw misalignment of 15° and 30°, they showed that the total power increased by 15% and 17% respectively. Ciri et al. [28] performed large-eddy simulations (LES) to evaluate yaw control for a three-turbine cascade. Using two different turbine sizes (NREL 5 MW reference turbine and Vestas V27, with 126 m and 27 m rotor diameters, respectively), the authors showed that a larger rotor diameter induces larger wake deflection, thus achieving higher power improvements. Power was maximized in the LES simulation using coordinated extremum seeking control [29].

As illustrated above, most of the efforts so far have focused on the impact of yaw misalignment in wind farms for enhancing the mean power output. The Levelized Cost of Energy (LCOE) of any wind farm is determined not only by energy production but also influenced by the stability of power output and maintenance of turbine structures. The wake deflection alters the turbulence statistics of flow (e.g., turbulence intensity, integral time scale, flow velocity spectra) impinging on downstream turbines and therefore their power output fluctuations. Moreover, the variation of wake flow direction and fluctuation intensities can highly impact the fatigue loading on downstream turbines, which is critical for the lifespan of turbines and their maintenance cost [30–34]. Indeed, for a 1.5 MW turbine, a 15% to 20% fatigue load reduction can reduce the LCOE by approximately 2.2% [35]. The understanding of fatigue loading on turbines will allow comprehensive evaluations of the impact of wake steering control on the LCOE of

the wind farm, and therefore determine the optimal yaw misalignment angle of individual turbines within the wind farm.

This investigation focuses on the fundamental coupling mechanism between wake flows, power output fluctuations, and unsteady aerodynamic loads on turbines with a wind farm under yaw misalignment. Systematic wind tunnel experiments with model turbines were performed to quantify the unsteady power outputs, thrust, and side forces on each row of turbines with various yaw misalignment angles. Furthermore, a reduced-order physical model based on the local incoming flow statistics and turbine properties was implemented to highlight the dominating factors for modulating the fluctuations of turbine power output and aerodynamic loads. To the best of the authors' knowledge, this is the first study that provides a comprehensive analysis of the power and wind load fluctuations for turbines within a wind farm under yaw misalignment with integrated experimental campaigns and modeling. This work is important for filling the current knowledge gap of predicting and controlling the power output stability as well as turbine fatigue loading when applying wake steering at a wind farm. The manuscript is organized as follows: Section 2 describes the experimental setup; Section 3 illustrates the results and discussions; conclusions are summarized in Section 4. An Appendix with the nomenclature used in the paper is also included.

2. Experimental setup

Wind tunnel experiments with two wind farm layouts, aligned and staggered, were performed to investigate the influence of yaw misalignment on turbine power output, aerodynamic load, and wake statistics. Model wind turbines with a yaw mechanism were placed on the bottom wall of the Boundary Layer and Subsonic Tunnel (BLAST) at the University of Texas at Dallas. The test section of BLAST is 2.1 m high, 2.8 m wide, and 30 m long. More details of the wind tunnel are provided in recent works [36-38]. To develop the turbulent boundary layer (TBL) for this study, roughness elements composed of cylindrical blocks with 2.5 cm diameter and 3 cm height were placed on the bottom surface of the test section (Fig. 1a). The rotation speed of the fan of BLAST was fixed at 120RPM; this led to the mean velocity of incoming flow at the hub height of the turbine as $U_{hub} = 7 \text{ m s}^{-1}$, and the turbulence intensity as $I_u = \sigma_u/U_{hub} = 9\%$. Here, σ_u denotes the standard deviation of the stream-wise velocity. Details of the boundary layer flow statistics are illustrated in Fig. 2.

The horizontal-axis wind turbines were designed based on the model from Bastankah et al. [39] and manufactured from the Stratasys F370 3D printer at the University of Texas at Dallas. All modeled turbines share the same rotor diameter of $d_T = 200$ mm and the hub height $z_{huh} =$ 200 mm, leading to a Reynolds number of $Re = U_{hub}d_T/v = 1.43 \times 10^5$; here ν is the kinematic viscosity of air. The turbine tower was made from M10 threaded rod. Details of the turbine blade geometry across various sections are provided in Bastankah et al. [39]. DCX16L Maxxon motors with a diameter of 16 mm attached with a 1 Ohm resistance were used as the loading to control the rotating speed of all the turbines. This led to tip-speed-ratio of $\lambda = \pi \omega d_T/U_{hub} \approx 4$ with power coefficient of $C_p = 0.35$ and thrust coefficient of $C_T = 0.8$ respectively in the free stream condition. Two wind farm layouts composed of these model turbines with three rows and three columns were tested in this work. The aligned layout had a stream-wise distance of $5d_T$ between each turbine row and a side-wise distance of $4d_T$ between each turbine column (Fig. 1b, (d); the staggered layout shared the same streamwise and side-wise distances between turbines but alternate rows were staggered by $2d_T$ (Fig. 1c, e). This led to the blockage ratio of the wind farm as 0.53% based on the rotor sweeping area and wind tunnel cross-section, which produced negligible blockage effects. In this work, special attention was focused on the influence of yaw misalignment on turbine performance. Here, the yaw angle of the first row turbines was changed from $\psi_{row1} \in [0^{\circ}, 45^{\circ}]$ with a step of $\Delta \psi = 5^{\circ}$, while that of the second row was adjusted ranging from $\psi_{row2} \in [-30^{\circ}, 30^{\circ}]$ with

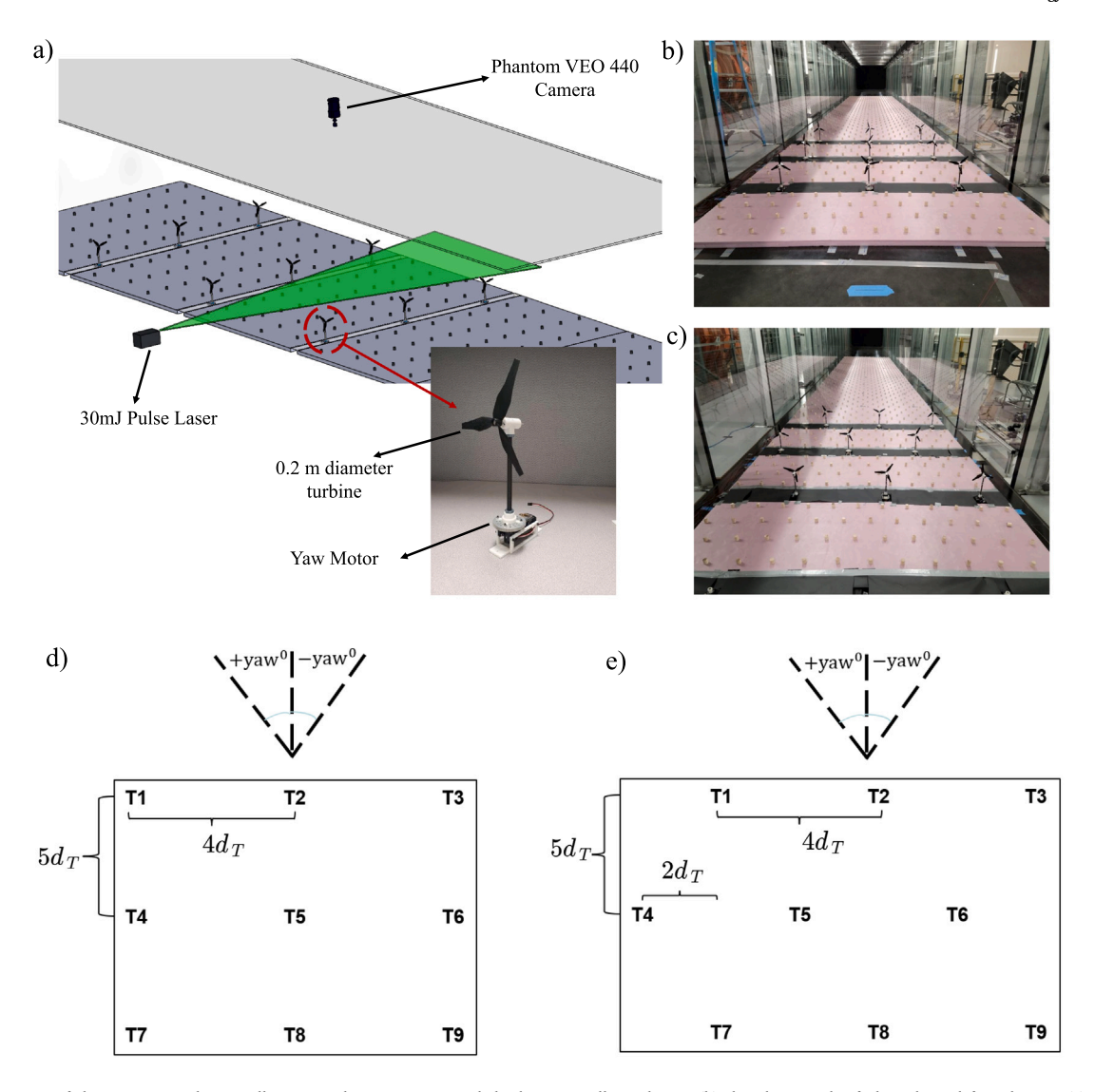


Fig. 1. (a) Schematic of the experimental setup illustrating the PIV system and the bottom wall roughness; (b) the photograph of aligned wind farm layout; (c) the photograph of staggered wind farm layout; (d) and (e) show the schematics of aligned and staggered layout respectively, where d_T is the turbine diameter.

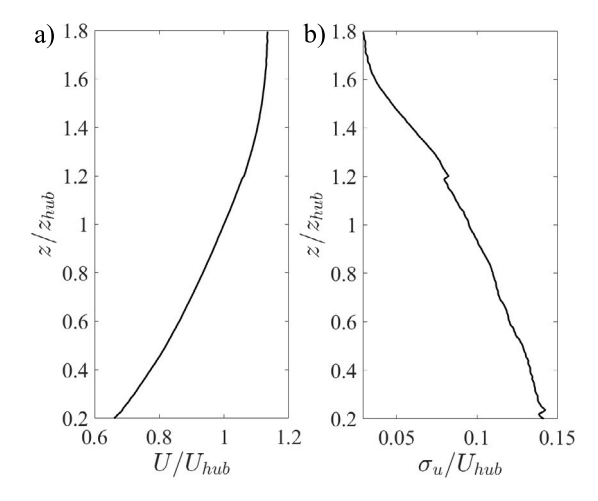


Fig. 2. Statistics of incoming turbulent boundary layer flow. (a) time-averaged velocity U/U_{hub} ; (b) stream-wise turbulence intensity σ_u/U_{hub} . The vertical distances are normalized by the turbine hub height z_{hub} .

Table 1
Summary of parameters for the experiment.

Summary of parameters for the experiment			
Description	Symbol	Quantity	Unit
Turbine diameter	d_T	200	mm
Turbine hub height	z_{hub}	200	mm
Mean incoming velocity at hub height	U_{hub}	7	m/s
Turbulence intensity at hub height	I_u	9	%
Reynolds number	Re	1.43×10^{5}	-
Coefficient of power	C_p	0.35	-
Coefficient of thrust	C_T	0.8	-
Tip speed ratio	λ	4	-
Yaw angle of first row turbine	ψ_{row1}	[0-45]	degree
Yaw angle of second row turbine	ψ_{row2}	[-30-30]	degree

the same step; this resulted in 130 yaw misalignment combinations for both aligned and staggered layouts (the third-row turbine was not yawed in this work). The yaw mechanism for each turbine was designed using Actobotics SG-12 series gearbox and was controlled using Arduino Mega and Laboratory Virtual Instrument Engineering Workbench (LabVIEW). More details of this mechanism can be found in Kumar et al. [40]. Table 1 summarizes the main parameters for our experiments.

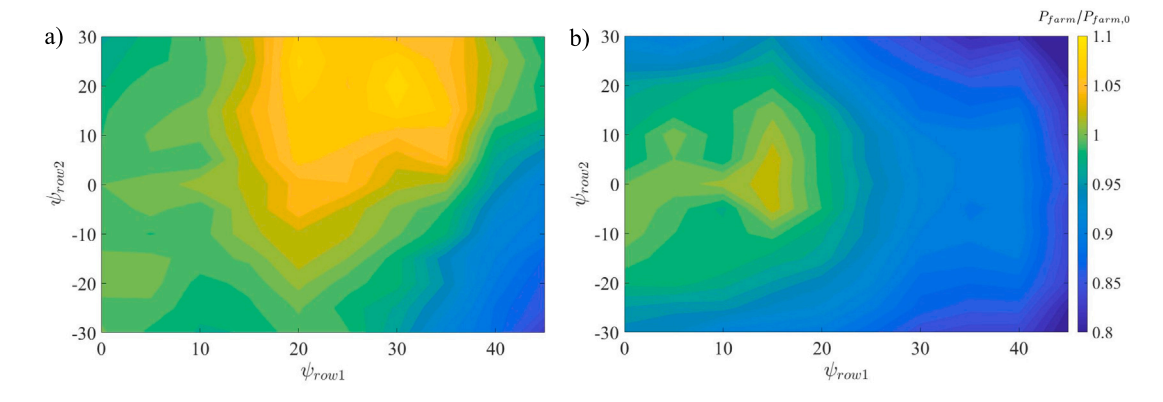


Fig. 3. Mean wind farm power output normalized by the base case, $P_{farm}/P_{farm,0}$ across various turbines yaw angles for (a) aligned layout and (b) staggered layout, where ψ_{row1} and ψ_{row2} are the yaw angles of first and second rows respectively.

The instantaneous turbine power output was inferred by the voltage of DC motors measured directly via a USB-6210 data logger from National Instruments. For each experiment, the voltage was sampled at a frequency of 10 kHz for a period of 60 s. In addition, we investigated the unsteady aerodynamic loads on the tower, which is an essential part of the turbine with 30% of the turbine's net cost, where any damage to the tower may impact all the other parts located on top of that [30]. The measurements of wind loading were achieved by an ATI Industrial Automation high-resolution force sensor connected to the turbine tower. The sensor was embedded within the bottom roughness to avoid any disturbance in the wake development. During each experiment, the instantaneous wind loads including thrust (the force aligned with the incoming flow direction) and side force (the force perpendicular to the incoming flow direction) were captured at a frequency of 1k Hz for periods of 60 s. The uncertainty of the sensor was less than 1.2%. In this work, the measurements of aerodynamic loads ranged within $\psi_{row1} \in [0^{\circ}, 30^{\circ}]$ and $\psi_{row2} \in [-30^{\circ}, 30^{\circ}]$. The incoming turbulent boundary layer and wake statistics downstream of the first-row turbine at $\psi_{row1} = 0^{\circ}, 10^{\circ}, 0^{\circ}$ and 30° were characterized by a time-resolved particle image velocimetry (PIV) system from TSI. A high-speed Phantom VEO440 camera with 4 MP resolution was used to create a field of view (FOV) of 400 mm × 200 mm to investigate the mean and unsteady wake flows. The FOV in the turbine wake region was parallel to the bottom wall and located within a streamwise distances of $x/d_T \in [3.2, 5.2]$ and side-wise distance of $y/d_T \in$ [-0.5, 0.5], where the coordinate system was defined with the origin coincident with the rotor center. The FOV for the incoming boundary layer flow has the same size as those within the turbine wake region but is perpendicular to the bottom wall. The FOV was illuminated by a 1 mm thick laser sheet generated from a 30 mJ/pulse laser, where airflow was seeded by 15 μ m-diameter soap bubbles from the TSI bubble generator. The soap bubbles were well mixed by the recirculating wind tunnel before each experiment. For each experiment, 6000 image pairs were collected at a frequency of 150 Hz. These image pairs were then processed using the Insight4G software package from TSI with a multi-pass scheme. The final interrogation window size was 32×32 pixels with 50% overlap, resulting in a final vector grid spacing $\Delta x =$ $\Delta y = 2.4$ mm. The overall uncertainty of the identified seeding particle locations was ~0.1 pixel; this led to the uncertainty of flow velocity measurement of ~1.4% given the bulk particle displacement of 7 pixels between two successive images.

3. Result and discussion

In this section, we discuss in detail the distinctive influences of turbine yaw misalignment on the power output, aerodynamic loads, and wake statistics within the model wind farms. Special attention will focus on downstream turbine power output fluctuations and unsteady wind loads with both experimental measurements and modeling.

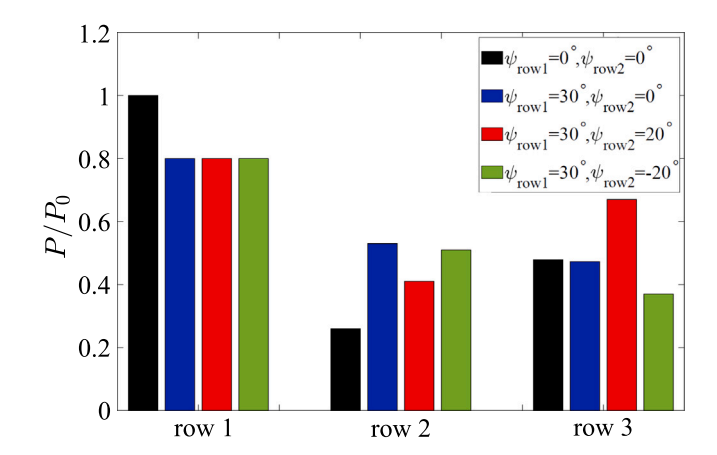


Fig. 4. Normalized power output of individual turbines, P/P_0 for representative cases. P_0 is the power of the first-row turbine at $\psi_{row1}=0^\circ$, where ψ_{row1} and ψ_{row2} are the yaw angles of the first and second rows respectively.

3.1. Layout-dependent wind farm power output

First, the time-averaged wind farm power output P_{farm} for the aligned layout normalized by the base case (i.e., $\psi_{row1} = \psi_{row2} = 0^{\circ}$), $P_{farm,0}$, is shown in Fig. 3a. The results indicate that wind farm power output is effectively modulated by the variation of turbine yaw angles in both the first and second rows. Specifically, with ψ_{row2} fixed at 0°, P_{farm} gradually increased with ψ_{row1} and reached the local maximum of $P_{farm}/P_{farm,0}=1.05$ at $\psi_{row1}=25^{\circ}$, and then rapidly decreased with further growth of ψ_{row1} . As pointed out by previous studies [10,22], the yaw misalignment decreases the power output of the upstream turbine. However, the wake deflection allows higher wind speed impinging the downstream counterparts and therefore increases P_{farm} across the entire wind farm. This phenomenon is more clearly presented in Fig. 4 via the mean power of turbines in each row normalized by that of the first-row turbine at $\psi_{row1}=0^{\circ}$. Compared to the base case, at $\psi_{row1}=30^{\circ}$ and $\psi_{row2}=0^{\circ}$, the power of the first-row turbine decreased by 20%, while that of the second row increased by approximately 100%. The variation of turbine yaw angle in the second row allows further optimization of P_{farm} . Overall, with ψ_{row2} the same sign of ψ_{row1} (i.e., turbines in the first two rows yawing at the same orientation), the effective wind velocity impinging the third-row turbine significantly increased compared to cases only yawing first-row turbine, which results in the growth of P_{farm} . In such circumstances, the maximum P_{farm} was achieved at $\psi_{row1} = 30^{\circ}$ and $\psi_{row2} = 20^{\circ}$ with $P_{farm}/P_{farm,0} = 1.085$. This phenomenon is similar to what was reported in recent wind tunnel studies [22,41]. On the other hand, cases with $\psi_{row1} > 0$ and $\psi_{row2} < 0$ led to the cancellation of wake deflection effects produced by turbines

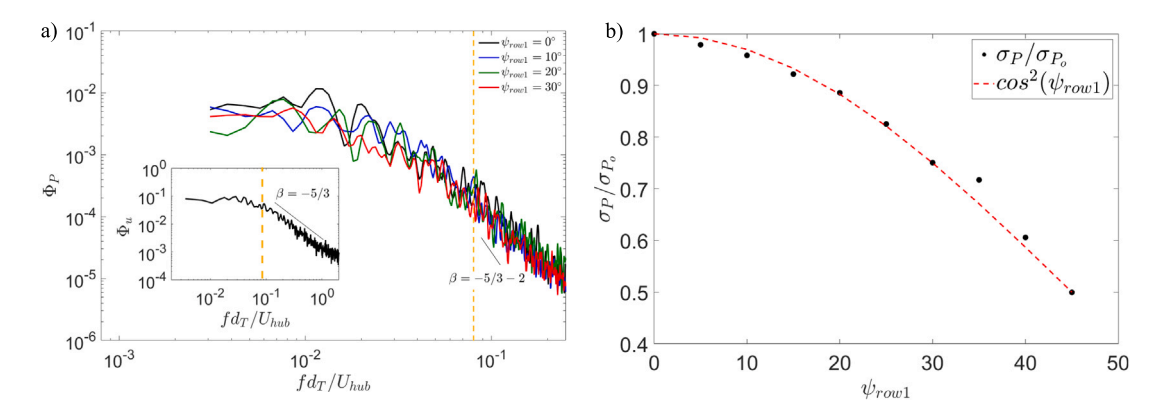


Fig. 5. (a) Power spectra, Φ_p , of first-row turbine across various yaw misalignment angles. The subplot shows the spectrum of incoming turbulent flow. (b) Standard deviation of power output normalized by the base case σ_P/σ_P of the first-row turbine, where ψ_{row1} is the yaw angles of the first row.

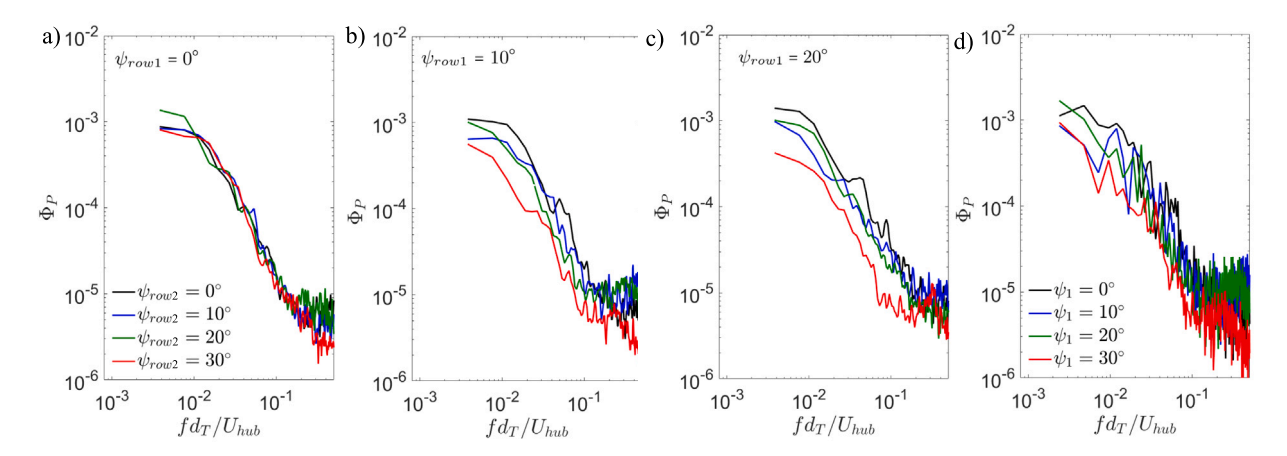


Fig. 6. Power spectra, Φ_p , of second-row turbine across various yaw misalignment angles under (a) $\psi_{row1} = 0^\circ$; (b) $\psi_{row1} = 10^\circ$; (c) $\psi_{row1} = 20^\circ$; (d) $\psi_{row1} = 30^\circ$, where ψ_{row1} and ψ_{row2} are the yaw angles of first and second rows respectively.

in first and second rows, where the power output of third-row turbine resulted to be even lower compared to the base case.

Compared to the wind farm with the aligned layout, the effectiveness of yaw misalignment was significantly suppressed for turbines with the staggered layout as illustrated in Fig. 3b. Here, the distribution of $P_{farm}/P_{farm,0}$ was approximately symmetric about $\psi_{row2}=0$, and maximum farm power increment was achieved at $\psi_{row1} = 15^{\circ}$ and $\psi_2 = 0^\circ$ with 2.5% growth compared to the base case. It is worth noting that for the wind farm with the staggered layout, the wake produced by the first-row turbine had minor influence on the secondrow counterpart and directly impinged on the third-row turbines. This resulted in the doubled stream-wise transport distance of wake flow compared to aligned cases, where its footprint was weakened and therefore had much less impact on downstream turbine performance. Considering that yaw misalignment was implemented to increase the wind farm power output, our following discussions for turbine power output fluctuations, aerodynamic loads, and wake statistics will focus on the wind farm with the aligned layout.

3.2. Power output fluctuations

Different from the mean power output which is governed by the local averaged incoming wind speed, the power fluctuations of turbines are influenced by more factors including turbulence intensity and integral time scales. In this work, we will characterize the turbine power output fluctuations in each row. First, Fig. 5(a) illustrates the spectra of instantaneous power outputs across various ψ_{row1} for the first-row turbine. Overall, all the Φ_P exhibited similar decaying trend

regardless of yaw angles, indicating that the scales of power output fluctuations is non-sensitive to yaw misalignment but dominated by the incoming turbulence. Indeed, the spectrum of incoming flow in the subplot of Fig. 5a shows that the inertial sub-range of turbulence started at $fd_T/U_{hub}\approx 0.08$; this corresponds to the distinct power-low decay with $\Phi_P\propto f^{-5/3-2}$ (marked with dashed yellow line) as reported in previous studies for turbines without yaw misalignment [42–44]. Meanwhile, the overall magnitude of Φ_P gradually decreased with the growth of the yaw misalignment angle across all frequency ranges. This phenomenon is more clearly reflected by the standard deviations of power output σ_P normalized by the base case σ_{P_0} in Fig. 5b, where σ_P decays with ψ_{row1} at a rate of $\sigma_P/\sigma_{P_0}\approx\cos^2(\psi)$ and followed a similar trend to that of mean power output as reported by previous studies [28].

Comparatively, yawing produced more impacts on power fluctuations for the second-row turbine (Fig. 6). In particular, for $\psi_{row1} \geq 10^\circ$, the growth of ψ_{row2} resulted in clear decrease of Φ_P across all frequency ranges. The variation of σ_P for second-row turbine across different ψ_{row1} and ψ_{row2} are summarized in Fig. 7a. Overall, with the growth of ψ_{row1} , σ_P of second-row turbine presented a distinctive increase; this trend indicated that yaw misalignment of upstream turbines produced both higher mean and unsteady power outputs of downstream counterparts. On the other hand, at a fixed ψ_{row1} , the maximum of σ_P was achieved at small $|\psi_{row2}|$. Interestingly, with the growth of ψ_{row1} , the local maximum of σ_P gradually shifted towards negative ψ_{row2} . This can be accounted to the span-wise components of wind flows impinging on second-row turbines due to wake steering, which altered the local mean velocity directions and will be further explained in the flow statistics.

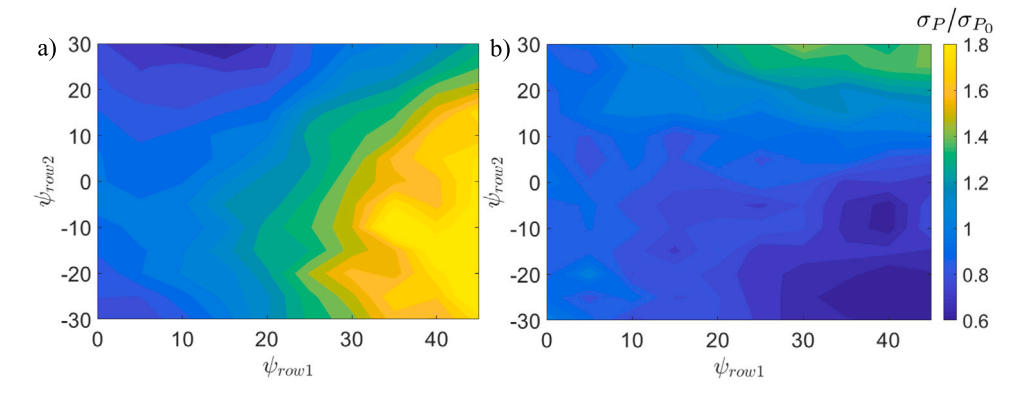


Fig. 7. Normalized standard deviation of power fluctuation σ_P/σ_{P_0} across various yaw angles for (a) second-row and (b) third-row turbines, where ψ_{row1} and ψ_{row2} are the yaw angles of first and second rows respectively.

Finally, the distribution of σ_P for the third-row turbine is exhibited in Fig. 7b. Overall, compared to that of the second-row counterpart, the power output fluctuations of the third-row turbine were not sensitive to both ψ_{row1} and ψ_{row2} , except a local maximum at $\psi_{row1} \rightarrow 30^\circ$ and $\psi_{row2} \rightarrow 30^\circ$. Following discussions about the coupling between wake statistics and power fluctuations will mostly focus on the second-row turbines.

3.3. Unsteady aerodynamic loads

The influence of yaw misalignment on unsteady aerodynamic loads acting on the first-row turbine tower was first characterized via the spectra of instantaneous wind forces as illustrated in Fig. 8. With the growth of ψ_{row1} , the magnitude of Φ_T for the first-row turbine gradually decreased (Fig. 8a); this is more clearly reflected via the standard deviation of thrust loads shown in the subplot of Fig. 8a, where σ_T reduced ~25% compared to the base case. Note that all the spectra of the first-row turbine presented similar trends, where Φ_T exhibited faster decay at $fd_T/Uhub \ge 0.08$ due to the modulation of turbulent flows as discussed in Fig. 5a. Compared to unsteady thrust loads, yaw misalignment induced much stronger impacts on side-force fluctuations. A monotonic upward shift of Φ_L with the growth of turbine yaw angle is clearly observed in Fig. 8b, where the standard deviation of side-force σ_L increased approximately 120% at $\psi_{row1} = 30^{\circ}$ compared to the base case (see the subplot). Note that the overall magnitude of Φ_L is much smaller compared to the corresponding Φ_T . To further analyze the coupling between unsteady thrust and side force, the joint probability density function (PDF) of instantaneous unsteady aerodynamic load coefficients, $C_{T'} = 2(T(t) - \bar{T})/(\rho A U_{hub}^2)$ and $C_{L'} =$ $2(L(t) - \bar{L})/(\rho A U_{hub}^2)$, are presented in Fig. 9. Here, T(t) and L(t) are instantaneous thrust and side-force at time t, whereas \bar{T} and \bar{L} are the mean thrust and side-force. In general, the unsteady aerodynamic loads exhibited two-dimensional Gaussian-style distribution; this is further validated with the fitting as

$$f(C_{T'}, C_{L'}) = (2\pi)^{-1} |\Sigma|^{-\frac{1}{2}} exp(-\frac{1}{2}F^T(\Sigma)^{-1}F)$$
 (1)

where $\Sigma = cov(C_{T'}, C_{L'})$ is the co-variance matrix of unsteady thrust and lift coefficients and $F = \begin{bmatrix} C_{T'} \\ C_{L'} \end{bmatrix}$ is the force coefficients vector. A sample of the fitted joint PDF based on Eq. (1) is shown in Fig. 9e for $\psi_{row1} = 30^{\circ}$, which well agrees with the measured result in Fig. 9d. Moreover, the dominating load fluctuations were always in the direction perpendicular to the rotor surface (marked as dashed red lines), and the force fluctuation intensity in this direction gradually decreased with the growth of the yaw angle. The results highlighted that the increase of side-force fluctuations with yaw angle is mostly attributed to the shifting of force fluctuation orientations.

The spectra of instantaneous wind forces acting on the secondrow turbine tower are illustrated in Fig. 10 for selected cases. For the

thrust loads, when the yaw angle of the first-row turbine is small, e.g., at $\psi_{row1} = 10^{\circ}$, the decaying of Φ_T started at $fd_T/U_{hub} \approx 0.2$ (Fig. 10a). This indicated that the velocity spectra within the wake flow are different from those of incoming turbulence. This value gradually decreased with the growth of ψ_{row1} and reached $f d_T/U_{hub} \approx 0.1$ at $\psi_{row1} = 30^{\circ}$ (Fig. 10b). Indeed, the yaw misalignment of the firstrow turbine deflected the wake flow and allowed the downstream turbine partially be impinged by the background turbulence, where the decaying trend of Φ_T gradually converged to those observed in the first row. It is worth noting that the delay of power spectra decay at small ψ_{row1} indicates that small-scale vortices are more energetic in the wake flow at small turbine vaw angles. This conclusion will be validated by flow measurements as discussed later. The spectra of sideforce fluctuations for second-row turbines are illustrated in Fig. 10c,d. In general, Φ_L presented a similar trend as a function of turbine yaw angle compared to the first-row counterparts, and the growth of Φ_L with ψ_{row2} became more distinctive at higher ψ_{row1} . The side-force fluctuation intensities for the second-row turbine can be more clearly reflected by the distribution of σ_L across various ψ_{row1} and ψ_{row2} as summarized in Fig. 11a. Overall, for the second-row turbine at any given ψ_{row1} , the growth of $|\psi_{row2}|$ led to higher σ_L , which corresponds to the upward shift of Φ_L observed in Fig. 10c,d. Also note that compared to turbine power fluctuations, the distribution of σ_L is lesssensitive to ψ_{row1} . This indicated that the impacts of different incoming flow statistics (e.g., mean velocity and turbulence intensity) due to yaw misalignment of the first-row turbine may cancel each other out, and the side-force fatigue loading on a turbine tower within a wind farm is dominated by its own yaw angles. We will further discuss this phenomenon with a theoretical model with the wake statistic measurements. Finally, the distribution of σ_L for the third-row turbine is illustrated in Fig. 11b, which exhibited negligible difference across all investigated ψ_{row1} and ψ_{row2} .

3.4. Wake flow statistics

In this section, we will quantify the influence of yaw misalignment on the mean velocity, turbulence intensity, velocity spectra, and integral time scales of wake flow. First, Fig. 12 shows mean normalized stream-wise velocity, U/U_{hub} , downstream of the first-row turbine at hub height with $\psi_{row1}=0^{\circ},10^{\circ},20^{\circ}$ and 30° . Overall, the yaw misalignment resulted in wake deflection away from the center line (i.e., y=0), and this deflection monotonously increased with the yaw angle. At the same time, due to the reduced projection area under yaw misalignment, the wake velocity deficit decreased compared to the base case, which led to higher mean velocity impinging on the downstream turbines and therefore increased their power output as discussed in Fig. 4. It is worth noting that yaw misalignment not only provided higher incoming velocities to the downstream turbine but also altered the wake flow

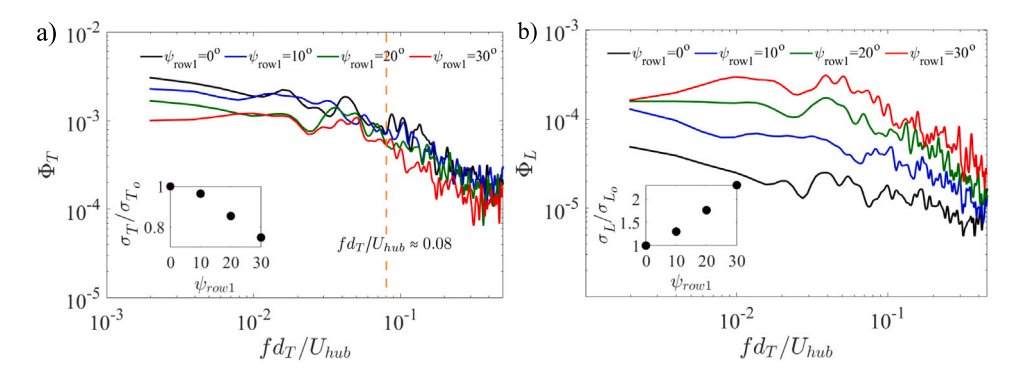


Fig. 8. Spectra of (a), Φ_T , thrust and (b), Φ_L , side-force of first row turbines within the wind farm, where ψ_{row1} is the yaw angle of first row turbines.

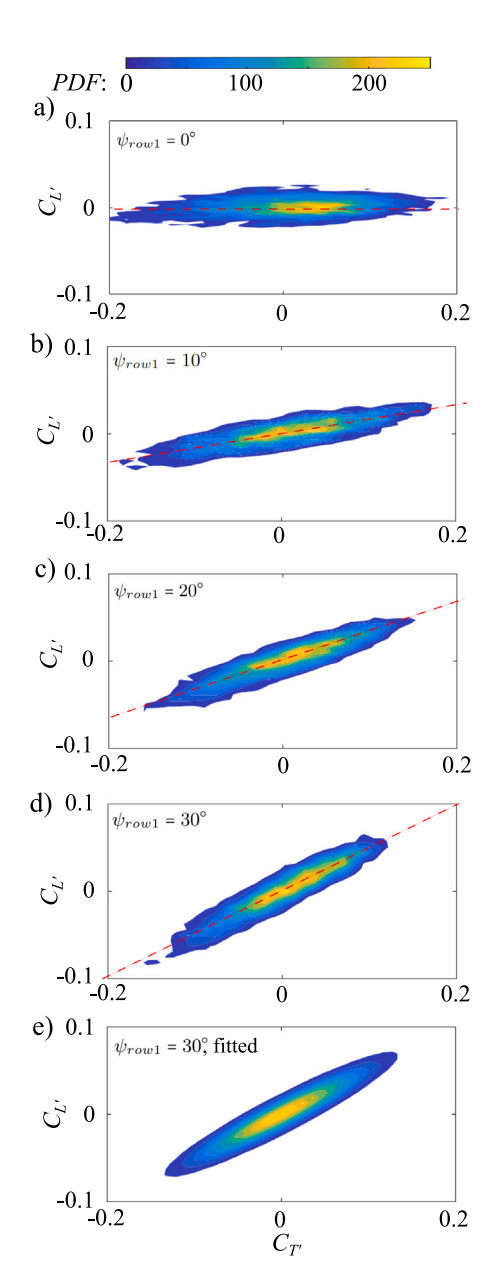


Fig. 9. Joint probability density function (PDF) of unsteady thrust (C_T') and side-force (C_L') for first-row turbine at (a) $\psi_{row1}=0^\circ$; (b) $\psi_{row1}=10^\circ$; (c) $\psi_{row1}=20^\circ$; (d) $\psi_{row1}=30^\circ$. (e) shows the fitting of joint PDF with Eq. (1) for $\psi_{row1}=30^\circ$.

directions; this can be more clearly observed via the superimposed streamlines, where a non-negligible span-wise flow with V<0 was generated (see Fig. 12d). In such a scenario, the wake impinging on the second-row troines will no longer be perpendicular to their rotor surfaces at $\psi_{row2}=0^\circ$. Moreover, the yaw misalignment angle between local incoming flow and rotor surface will be larger than $|\psi_{row2}|$ when $\psi_{row2}>0$, and smaller than $|\psi_{row2}|$ when $\psi_{row2}<0$.

The influence of yaw misalignment on wake fluctuations was first characterized by the distribution of turbulence intensity $I_{\nu} = \sigma_{\nu}/U_0$ in Fig. 13. Selected transverse profiles of I_{μ} at various downstream locations are also illustrated in Fig. 14. Indeed, due to the strong velocity shear right downstream of turbine tips at $\psi_{row1}=0^{\circ}$, the wake turbulence intensity presented local peaks at $y/d_T \pm 0.5$ and reached minimal at $y/d_T=0$. The growth of ψ_{row1} gradually deflected the peak at the leading edge side of the turbine towards the rotor center; in particular, this peak reached y=0 when ψ_{row1} increased to 30°. On the other hand, the overall turbulence intensity presented monotonic decay with the increase of ψ_{row1} . Interestingly, despite the smaller I_u under higher ψ_{row1} at $x/d_T = 5$ (i.e., the location of the second-row turbine), the second-row turbine presented larger σ_P compared to the base case as shown in Fig. 7a. This indicates that the wind velocity fluctuation intensity may not be the dominating factor for determining turbine power output fluctuations.

To further understand the effect of yaw misalignment on the scales of wake flow fluctuations, the pre-multiplied stream-wise velocity spectral difference between wake and incoming flows $\Delta(\phi f) = \phi f - \phi_{in} f$ at $x/d_T = 5$ is shown in Fig. 15 for various ψ_{row1} and span-wise locations. For the base case, the compensated spectra highlighted energy decrease within $f d_T/U_{hub} \in [0.02, 0.1]$ but distinctive energy increase at $f d_T/U_{hub} > 0.1$; this corresponds to the 'high-pass' filtering effect of turbine on wake flow statistics as reported in previous studies [36,45]. Note that close to y = 0, the 'high-pass' filtering effectiveness was stronger than other span-wise locations, indicating that the wake vortex scales reached the local minimal near the wake center line. As discussed in Fig. 12, the yaw misalignment deflected the wake center-line, where the 'high-pass' filtering effect was suppressed at the leading edge side of the first-row turbine (i.e., $y/d_T > 0$) but strengthened within $y/d_T < 0$. Finally, the evolution of turbulence integral time scale normalized by that of incoming flow T^u/T^u_{inc} , was presented in Fig. 16. Quantification of the spatial distribution of T^u within wake flow is essential for analyzing and predicting downstream turbine power output fluctuations. Here, T^u is computed via the integral of auto-correlation function $r(\epsilon)$ of local stream-wise velocity as:

$$T^{u} = \int_{0}^{\infty} \gamma(\epsilon) d\epsilon$$

$$\gamma(\epsilon) = \langle u'(t)u'(t - \epsilon) \rangle / \sigma_{u}^{2}$$
(2)

where ϵ is time lag and u' is the velocity fluctuation in stream-wise direction. Here, the integration was evaluated up to $r(\epsilon)$ is smaller than 0.1. For the base case (Fig. 16a), T^u is substantially reduced

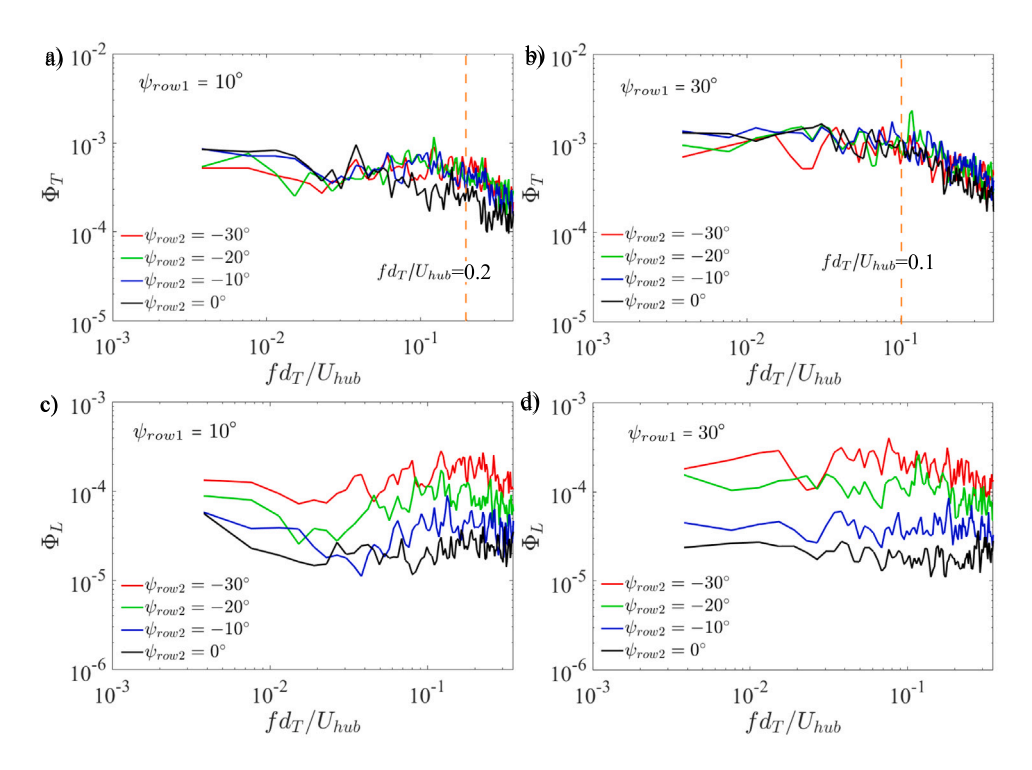


Fig. 10. Spectra of (a-b), Φ_T , thrust and (c-d), Φ_L , side-force of second-row turbines within the wind farm, where ψ_{row1} and ψ_{row2} are the yaw angles of first and second rows respectively.

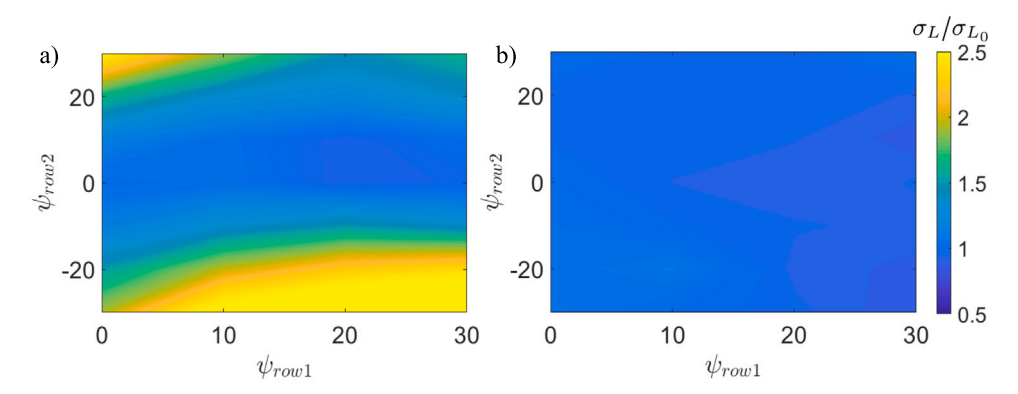


Fig. 11. Standard deviation of side-forces normalized by the base case σ_L/σ_{L_0} for (a) second and (b) third-row turbines, where ψ_{row1} and ψ_{row2} are the yaw angles of first and second rows respectively.

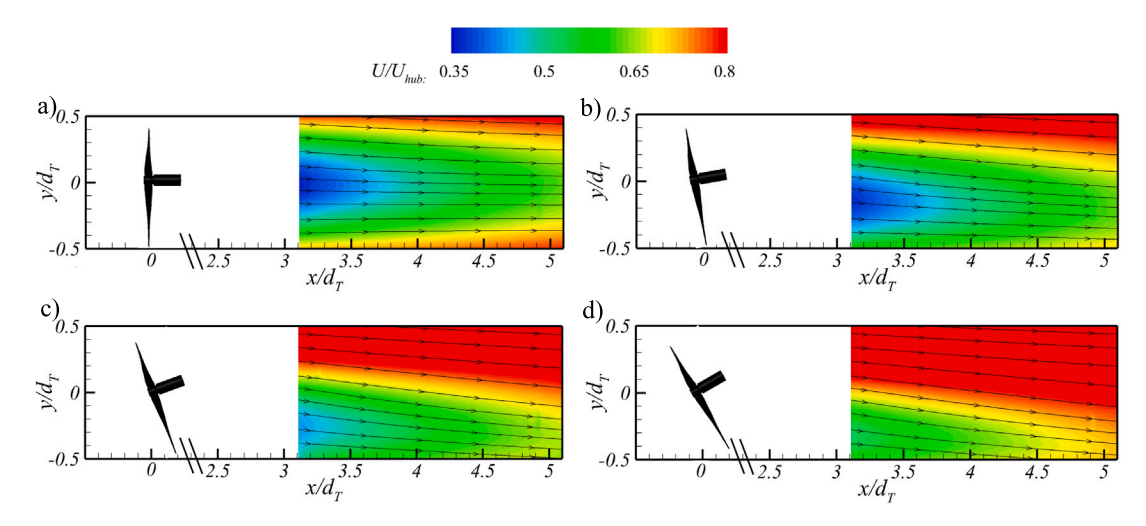


Fig. 12. Normalized mean stream-wise velocity distribution, U/U_{hub} , in the wake of first-row turbine at $\psi_{row1} = (a)~0^{\circ}$, (b) 10° , (c) 20° , and (d) 30° . The superimposed streamlines highlight the induced span-wise velocities at high yaw angles. Where x/d_T and y/d_T are the stream-wise and span-wise distances normalized by turbine diameter respectively.

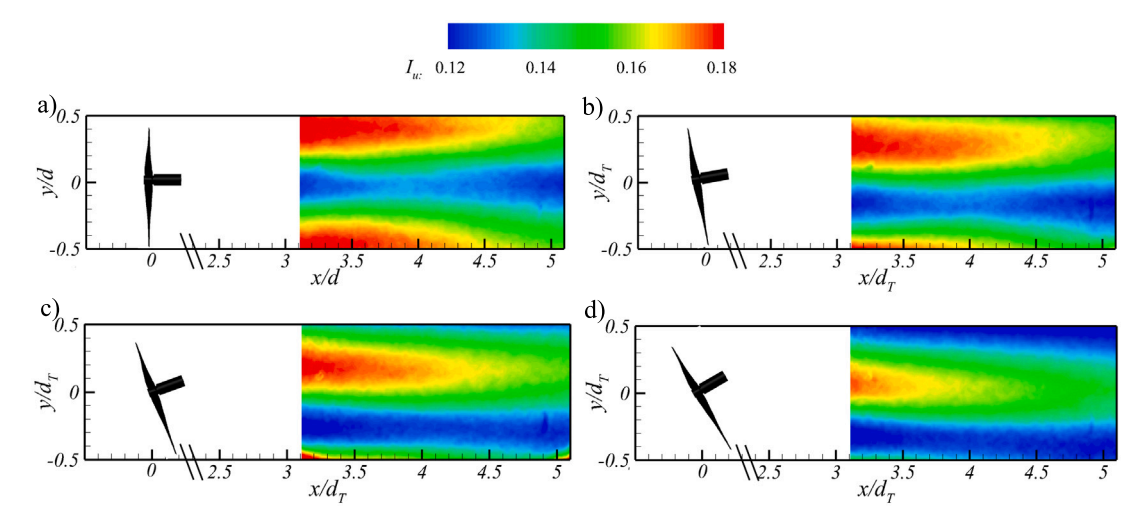


Fig. 13. Turbulence intensity distribution, I_u , in the wake of first-row turbine at $\psi_{row1} =$ (a) 0° , (b) 10° , (c) 20° , and (d) 30° . Where x/d_T and y/d_T are the stream-wise and span-wise distances normalized by turbine diameter respectively.

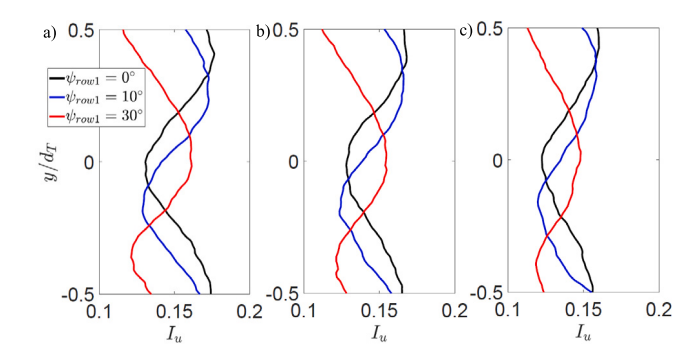


Fig. 14. Transverse profiles of the wake turbulence intensity, I_u , across different ψ_{row1} at (a) $x/d_T=4$; (b) $x/d_T=4.5$; (c) $x/d_T=5$.

compared to that of incoming flow with $T^u/T^u_{inc}\approx 0.4$ across the FOV. Note that a local minimum of T^u was observed within $x/d_T\in [4.5,5]$ near the wake center-line, which corresponds to the small wake vortex scales as illustrated in Fig. 15. Interestingly, this local minimal of T^u extended towards the upstream direction with the growth of ψ_{row1} , indicating that yaw misalignment not only deflected the direction of wake development but also suppressed large-scale vortices along the wake center-line.

3.5. Theoretical interpretation of power output fluctuations and unsteady aerodynamic loads

The experimental measurement has highlighted the significant impact of yaw misalignment on power output fluctuations and unsteady aerodynamic loads (especially the side-force component) for the second-row turbine under wake flow. In this section, we will further investigate these phenomena via reduced-order physical models. Here, we start with two simplifying assumptions. First, we assume that the unsteady power output or aerodynamic loads of a turbine are mainly induced by velocity fluctuations from incoming flow; the impact of wake dynamics, such as tip vortex shedding is not included in current work. Second, we assume that for turbines within a wind farm, the local incoming flow follows the Von Kármán turbulence model [46].

Based on the assumptions, the spectrum of turbine power output $\Phi_n(f)$ can be expressed as a function of velocity magnitude, turbulence

intensity, and integral time scale of incoming wind flow by Tobin *et*. *al.* [47] as:

$$\phi_p(f) = \frac{(3/2C_p\rho AU^2)^2}{\sqrt{1 + (2\pi ft)^4}} \frac{4\sigma_u^2 T^u}{(1 + 70.8(fT^u)^2)^{5/6}}$$
(3)

Here, $t_i = I\omega(2\tau)$ is the inertial time scale, I is the rotor inertia and τ is the electric torque. Due to the yaw misalignment, the wake velocity profile impinging on the second-row turbine presented distinctive variations along span-wise direction. In this work, all the wake statistic parameters (i.e., U, σ_u , and T^u) were obtained by the spatial average across the rotor span of the second-row turbine. In addition, the yaw misalignment will lead to a significant decrease in power output fluctuations. This trend can be approximated via $\sigma_P/\sigma_{P_0} \approx \cos^2|\psi|$ based on the results from Fig. 5b. In this model, ψ is considered as the misalignment angle between the directions of the local incoming wind and that perpendicular to the rotor surface. As discussed in Fig. 12, due to the yawing of first-row turbines, their wake flows were no longer parallel to the incoming winds; this factor was considered via the ratio between local mean stream-wise and span-wise wake velocities as $\alpha = atan(-V/U)$. Indeed, our experimental results showed that α can be up to 5° when ψ_{row1} increased to 30°, which accounted for the asymmetry of power output fluctuation contours with regard to $\psi_{row2} = 0^{\circ}$. By considering the effective yaw misalignment angle as $ψ_{row2} + α$ (see Fig. 17a), we can integrate $σ_P/σ_{P_o} \approx \cos^2 |ψ|$ into (3) as:

$$\phi_p(f) = \frac{(3/2C_p\rho AU^2\cos(\psi_{row2} + \alpha)^2)^2}{\sqrt{1 + (2\pi ft_i)^4}} \frac{4\sigma_u^2 T^u}{(1 + 70.8(fT^u)^2)^{5/6}}$$
(4)

The integral of Eq. (4) across all frequencies allows us to calculate the variance of power. The modeled and measured σ_P/σ_{P_o} for the second-row turbine across various ψ_{row1} and ψ_{row2} are presented in Fig. 18. The comparison is within the range of $\psi_{row1} \in [0^\circ, 30^\circ]$ due to the range of flow statistics measurement. In general, the model shows good agreement with the experimental measurements. Indeed, considering that the growth of ψ_{row1} produced higher U but lower σ_u in the wake flow, the overall increasing trend of σ_P with ψ_{row1} from both models and experiments illustrated that the variation of local mean velocity plays a more important role than that of turbulence intensity for modulating turbine power output fluctuations. Moreover, the model succeeded to predict the asymmetric distribution of σ_P with regards to ψ_{row2} at high ψ_{row1} regions, which is accounted for the existence of wake deflection angle α .

On the other hand, the variation of unsteady aerodynamic loads behaves as a more complex relationship with turbine yaw angle due to the coupling between thrust and side-force components. In this

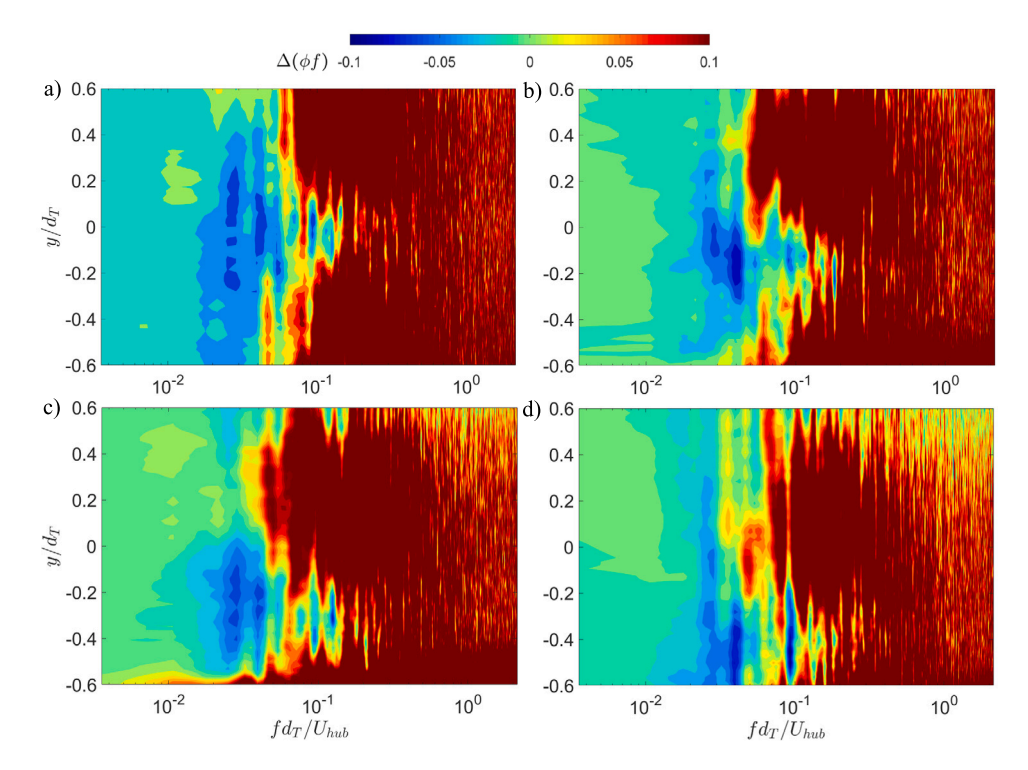


Fig. 15. Compensated velocity spectra, $\Delta(\phi f)$, at $x/d_T = 5$ with yaw angles of $\psi_{row1} = (a)~0^\circ$, (b) 10° , (c) 20° , and (d) 30° . where y/d_T are the span-wise distances normalized by turbine diameter respectively.

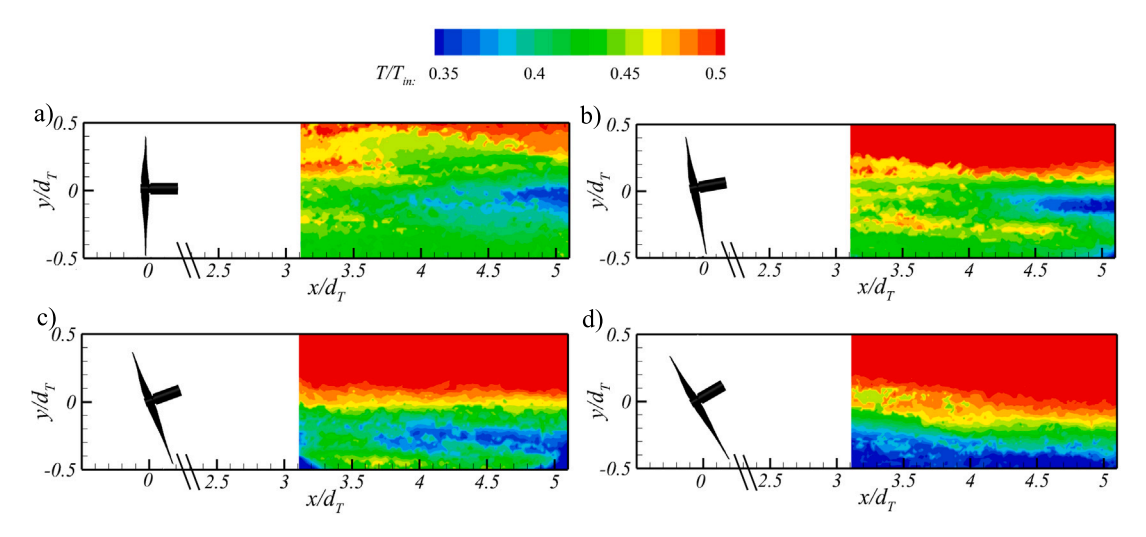


Fig. 16. Normalized Integral time scale, T_u in the wake of first-row turbine at $\psi_{row1} = (a)~0^{\circ}$, (b) 10° , (c) 20° , and (d) 30° . Where x/d_T and y/d_T are the stream-wise and span-wise distances normalized by turbine diameter respectively.

work, we consider that σ_L of the second-row turbine is dominated by three factors, namely, the flow fluctuation intensity, the rotor surface orientation, and the relative angle between local incoming flow and rotor surface. First, for a turbine under turbulent incoming flow, its instantaneous aerodynamic loads $F_a(t)$ in any direction can be considered as

$$F_a(t) = 1/2C_F \rho A(U + u'(t))^2$$

= 1/2C_F \rho A(U^2 + 2Uu'(t) + u'(t)^2) (5)

where C_F denotes the aerodynamic load coefficient. Considering that $|U| \gg |u'(t)|$, as a first-order approximation, the fluctuation term of $F_a(t)$ is dominated by the term of Uu'(t) as

$$\sigma_F \propto U \sigma_u$$
 (6)

Secondly, as discussed in Fig. 9, the joint PDF of unsteady force can be considered as a 2D Gaussian distribution, where the dominating force fluctuations are always in the direction perpendicular to the rotor surface regardless of yaw angles. Therefore, to facilitate the decoupling of aerodynamic loads, we consider the unsteady wind loads in the rotated coordinate system x' - y', where x' denotes the direction perpendicular to the rotor surface and y' is the one parallel to the rotor (Fig. 17a). This leads to

$$N' = T' \cos \psi_{row2} + L' \sin \psi_{row2}$$

$$R' = -T' \sin \psi_{row2} + L' \cos \psi_{row2}$$
(7)

Here, N' is the unsteady rotor normal force and R' is the one at the rotor parallel direction. In such a scenario, the covariance coefficient

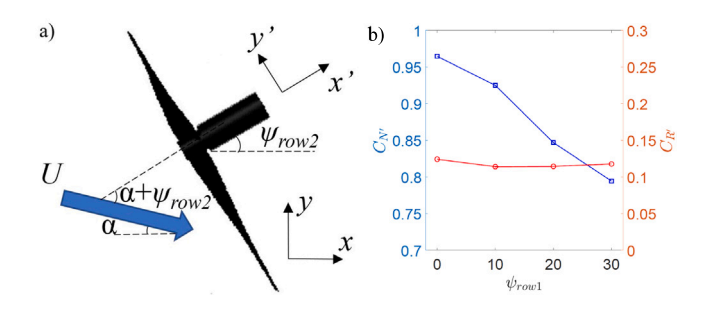


Fig. 17. (a) Schematic of local incoming flow, rotor surface, and rotated coordinate system for the second-row turbine. (b) Distribution of unsteady normal force coefficient, $C_{N'}$, and radial force coefficient, $C_{R'}$, as a function of yaw angle, ψ_{row1} . α , is the incoming flow direction to second row turbine and ψ_{row2} is the yaw angle of second row turbine.

between N' and R' is small and the joint PDF can be determined by just using the standard deviation of N' and R' (i.e., σ_N and σ_R) as:

$$f(N', R') = \frac{1}{2\pi\sigma_N \sigma_R} exp(-\frac{1}{2} [(\frac{N'}{\sigma_N})^2 + (\frac{R'}{\sigma_R})^2])$$
 (8)

To facilitate the quantification of σ_N and σ_R as a function of yaw misalignment and local incoming turbulent flow, we redefine the unsteady aerodynamic load coefficients as

$$\begin{split} C_{N'}(\psi) &= \frac{2\sigma_N(\psi)}{\rho A U \sigma_u} \\ C_{R'}(\psi) &= \frac{2\sigma_R(\psi)}{\rho A U \sigma_u} \end{split} \tag{9}$$

Note that this definition is based on the relationship of $\sigma_F \propto U\sigma_u$. Fig. 17b shows the variation of $C_{N'}$ and $C_{R'}$ as a function of the yaw angle from the first-row turbine. As expected, $C_{N'}$ decreased with the growth of ψ_{row1} , which corresponds to the mitigated force fluctuation intensity in the rotor normal direction as observed from Fig. 9. Meanwhile, $C_{R'}$ remained a constant regardless of the yaw angle. Then, considering the effective yaw angle $\psi_{row2} + \alpha$ of second row turbine, its σ_N and σ_R can be approximated as:

$$\sigma_{N} = \frac{1}{2} C_{N'}(|\psi_{row2} + \alpha|) \rho A U \sigma_{u}$$

$$\sigma_{R} = \frac{1}{2} C_{R'}(|\psi_{row2} + \alpha|) \rho A U \sigma_{u}$$
(10)

where the values of $C_{N'}$ and $C_{R'}$ are obtained via the interpolation from Fig. 17b.

Finally, with the joint PDF in the x'-y' coordinate system from Eqs. (8) to (10), the standard deviation of loads in y direction (i.e., σ_L) is calculated as:

$$\sigma_L = \sqrt{\int f(N', R')(N'\sin\psi_{row2} + R'\cos\psi_{row2})^2 dN'dR'}$$
 (11)

The modeled σ_L from Eq. (11) normalized by the base case are compared with the experimental results in Fig. 19. Note that the case of $\psi_{row2}=30^\circ$ is not included for comparison because $|\psi_{row2}+\alpha|$ can be larger than 30°, which is beyond the interpolation range of measured $C_{N'}$ and $C_{R'}$. Overall, the model agrees well with the experimental results. Note that for cases under high $|\psi_{row2}|$, the asymmetric wake patterns from the leading and trailing edge of the turbine rotor may lead to an additional disturbance on unsteady aerodynamic loads, which can be the reason for overestimation of σ_L from the model. The models for both σ_P and σ_L highlighted that $\sigma_P \propto U^2 \sigma_u$ but $\sigma_L \propto U \sigma_u$. This explained the phenomenon that for the second-row turbine, σ_L is less sensitive to the variation of ψ_{row1} compared to that of σ_P since both

mean velocity and turbulence intensity have similar weights to σ_L and the impacts of these two factors cancel each other out.

4. Conclusion

Wind tunnel experiments were performed to investigate the unsteady power output and aerodynamic load fluctuations of turbines within wind farms under yaw misalignment. A three-row and threecolumn wind farm consisting of miniature wind turbines was studied for both aligned and staggered layouts. Results highlighted that yaw misalignment is much more effective for increasing wind farm power output with an aligned layout. The investigation on aligned wind farms showed that the decaying rates of power output spectra are highly modulated by the local turbulent incoming flow. Overall, the growth of yaw misalignment reduces turbine power fluctuation intensities. However, this action can increase the power fluctuations of downstream turbines due to the higher incoming wind speeds. Measurements of the unsteady aerodynamic loads on the turbine tower illustrated that yaw misalignment can significantly increase the side-force fatigue loading across all frequencies. In general, the unsteady aerodynamic loads present a 2D Gaussian distribution, and the dominating unsteady loads are always in the direction perpendicular to the rotor surface regardless of the turbine yaw angle.

The investigation of wake characteristics revealed that with the growth turbine yaw angles, the flows can be significantly deflected, which results in the increase of wake velocities, integral time scales, and a decrease in turbulence intensity. Based on the flow statistics, reduced-order models were established to elucidate the evolution of downstream turbine power output fluctuations and unsteady wind loads. Results revealed that these parameters are dominated by the coupled impacts of local wind speed and turbulence intensity. Specifically, the variation of wind speed is the governing factor for power fluctuations, while both wind speed and turbulence intensity have similar impacts in determining unsteady aerodynamic loads, which makes the side-force fluctuations not sensitive to upstream turbine yaw angles. To sum up, this work revealed the fundamental mechanisms modulating the power fluctuations and unsteady wind loads on turbines under yaw misalignment via combined experimental campaigns and theoretical modeling. Subsequent work aims to tackle wind farms under complex terrains and the fatigue aerodynamic loads on turbine blades.

CRediT authorship contribution statement

Emmanuvel Joseph Aju: Conceptualization, Methodology, Data analysis, Original draft preparation. Devesh Kumar: Conceptualization, Methodology, Data analysis. Melissa Leffingwell: Methodology. Mario A. Rotea: Conceptualization, Supervision, Reviewing and editing. Yaqing Jin: Conceptualization, Supervision, Reviewing and editing.

Declaration of competing interest

The authors declare that they have no known competing financial interests or personal relationships that could have appeared to influence the work reported in this paper.

Acknowledgments

This material is based upon work supported by the National Science Foundation, United States under Award Number 1916776, Phase II I/UCRC at UT Dallas: Center for Wind Energy Science, Technology and Research (WindSTAR) and the WindSTAR UCRC Members, United States. Any opinions, findings, conclusions, or recommendations expressed in this material are those of the authors and do not necessarily reflect the views of the National Science Foundation or WindSTAR members.

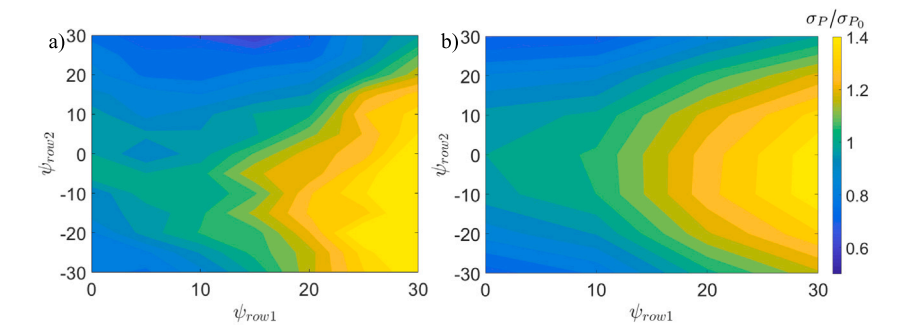


Fig. 18. Normalized standard deviation of power fluctuation σ_P/σ_{P_0} , of second-row turbine. (a) Measured (b) Modeled. Where ψ_{row1} and ψ_{row2} are the yaw angles of the first and second rows respectively.

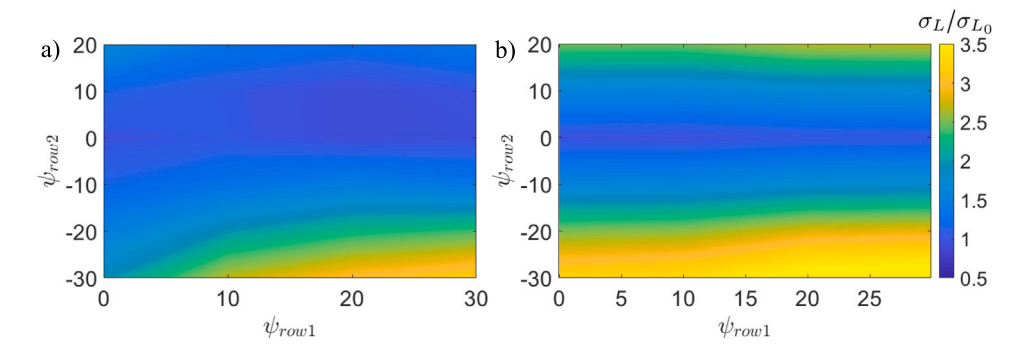


Fig. 19. Normalized standard deviation of side-force fluctuation σ_L/σ_{L_0} , of second-row turbine. (a) Measured (b) Modeled. Where ψ_{row1} and ψ_{row2} are the yaw angles of the first and second rows respectively.

Appendix. Nomenclature

Incoming Flow Direction to Second Row Turbine
Tip Speed Ratio
Power Spectral Density of Side-Force
Power Spectral Density of Power output
Power Spectral Density of Thrust-Force
Yaw angle of first row turbine
Yaw angle of second row turbine
Air Density
Standard Deviation of Side-Force
Standard Deviation of Power
Standard Deviation of Thrust-Force
Standard Deviation of Stream-wise Velocity
Coefficient of Side-Force fluctuations
Coefficient of Side-Force
Coefficient of Rotor-Normal Force fluctuations
Coefficient of Power
Coefficient of Rotor-Parallel Force fluctuations
Coefficient of Thrust fluctuations
Coefficient of Thrust
Turbine Diameter
Frequency
Aerodynamic Load
Turbulecne Intensity at hib Height
Side-Force of turbine
Rotor-Normal Force of turbine
Power output of turbine
Power output of wind farm
Probability Density Function
Rotor-Parallel Force of turbine
Reynolds Number

T	Thrust Force of turbine
T^u	Integral Time Scale
t_i	Inertial Time Scale
U_{hub}	Mean Incoming Velocity at Hub Height
X	Stream-Wise Distance
y	Span-Wise Distance
z_{hub}	Turbine Hub Height

References

- Electricity in the United States Energy Explained, Your Guide to Understanding Energy, EIA, 2019, https://www.eia.gov/energyexplained/index.cfm?page= electricity_in_the_united_states.
- [2] Matthew Churchfield, Sang Lee, Patrick Moriarty, Luis Martinez, Stefano Leonardi, Ganesh Vijayakumar, James Brasseur, A large-eddy simulation of windplant aerodynamics, in: 50th AIAA Aerospace Sciences Meeting Including the New Horizons Forum and Aerospace Exposition, 2012, p. 537.
- [3] Rebecca Jane Barthelmie, K. Hansen, Sten Tronæs Frandsen, Ole Rathmann, J.G. Schepers, W. Schlez, J. Phillips, K. Rados, A. Zervos, E.S. Politis, et al., Modelling and measuring flow and wind turbine wakes in large wind farms offshore, Wind Energy 12 (5) (2009) 431–444.
- [4] Robert Mikkelsen, Jens N. Sørensen, Stig Øye, Niels Troldborg, Analysis of power enhancement for a row of wind turbines using the actuator line technique, in: Journal of Physics: Conference Series, Vol. 75, IOP Publishing, 2007, 012044.
- [5] I. Grant, P. Parkin, X. Wang, Optical vortex tracking studies of a horizontal axis wind turbine in yaw using laser-sheet, flow visualisation, Exp. Fluids 23 (6) (1997) 513–519.
- [6] Ian. Grant, P. Parkin, A dpiv study of the trailing vortex elements from the blades of a horizontal axis wind turbine in yaw, Exp. Fluids 28 (4) (2000) 368–376.
- [7] Davide Medici, P.H. Alfredsson, Measurements on a wind turbine wake: 3d effects and bluff body vortex shedding, Wind Energy 9 (3) (2006) 219–236.
- [8] Paul A. Fleming, Pieter M.O. Gebraad, Sang Lee, Jan-Willem van Wingerden, Kathryn Johnson, Matt Churchfield, John Michalakes, Philippe Spalart, Patrick Moriarty, Evaluating techniques for redirecting turbine wakes using sowfa, Renew. Energy 70 (2014) 211–218.
- [9] Ángel Jiménez, Antonio Crespo, Emilio Migoya, Application of a les technique to characterize the wake deflection of a wind turbine in yaw, Wind Energy 13 (6) (2010) 559–572.
- [10] Majid Bastankhah, Fernando Porté-Agel, Experimental and theoretical study of wind turbine wakes in yawed conditions, J. Fluid Mech. 806 (2016) 506–541.

- [11] Michael F. Howland, Juliaan Bossuyt, Luis A. Martínez-Tossas, Johan Meyers, Charles Meneveau, Wake structure in actuator disk models of wind turbines in yaw under uniform inflow conditions, J. Renew. Sustain. Energy 8 (4) (2016) 043301
- [12] M. Churchfield, Qi Wang, A. Scholbrock, T. Herges, T. Mikkelsen, Mikael. Sjöholm, Using high-fidelity computational fluid dynamics to help design a wind turbine wake measurement experiment, in: Journal of Physics: Conference Series, Vol. 753, IOP Publishing, 2016, 032009.
- [13] J. Wang, S. Foley, E.M. Nanos, T. Yu, Filippo Campagnolo, Carlo Luigi Bottasso, Alex Zanotti, Alessandro Croce, Numerical and experimental study of wake redirection techniques in a boundary layer wind tunnel, in: Journal of Physics: Conference Series, Vol. 854, IOP Publishing, 2017, 012048.
- [14] Carl R. Shapiro, Dennice F. Gayme, Charles Meneveau, Modelling yawed wind turbine wakes: a lifting line approach, J. Fluid Mech. 841 (2018).
- [15] Jannik Schottler, Jan Bartl, Franz Mühle, Lars Sætran, Joachim Peinke, Michael Hölling, Wind tunnel experiments on wind turbine wakes in yaw: redefining the wake width. Wind Energy Sci. 3 (1) (2018) 257–273.
- [16] M. Bastankhah, F. Porté-Agel, Wind tunnel study of the wind turbine interaction with a boundary-layer flow: Upwind region, turbine performance, and wake region, Phys. Fluids 29 (6) (2017) 065105.
- [17] Majid Bastankhah, Fernando Porté-Agel, A wind-tunnel investigation of wind-turbine wakes in yawed conditions, in: Journal of Physics: Conference Series, Vol. 625, IOP Publishing, 2015, 012014.
- [18] Ahmet Ozbay, Wei Tian, Zifeng Yang, Hui Hu, Interference of wind turbines with different yaw angles of the upstream wind turbine, in: 42nd AIAA Fluid Dynamics Conference and Exhibit, 2012, p. 2719.
- [19] Jan Bartl, Franz Mühle, Jannik Schottler, Lars Sætran, Joachim Peinke, Muyiwa Adaramola, Michael Hölling, Wind tunnel experiments on wind turbine wakes in yaw: effects of inflow turbulence and shear, Wind Energy Sci. 3 (1) (2018) 329–343.
- [20] M.F. Howland, S.K. Lele, J.O. Dabiri, Wind farm power optimization through wake steering, Proc. Natl. Acad. Sci. USA 116 (29) (2019) 14495–14500.
- [21] Filippo Campagnolo, Vlaho Petrović, Johannes Schreiber, Emmanouil M. Nanos, Alessandro Croce, Carlo L. Bottasso, Wind tunnel testing of a closed-loop wake deflection controller for wind farm power maximization, in: Journal of Physics: Conference Series, Vol. 753, IOP Publishing, 2016, 032006.
- [22] Haohua Zong, Fernando Porté-Agel, Experimental investigation and analytical modelling of active yaw control for wind farm power optimization, Renew. Energy 170 (2021) 1228–1244.
- [23] Pieter M.O. Gebraad, Matthew J. Churchfield, Paul A. Fleming, Incorporating atmospheric stability effects into the floris engineering model of wakes in wind farms, in: Journal of Physics: Conference Series, Vol. 753, IOP Publishing, 2016, 052004.
- [24] J. Schreiber, B. Salbert, C.L. Bottasso, Study of wind farm control potential based on scada data, in: Journal of Physics: Conference Series, Vol. 1037, IOP Publishing, 2018, 032012.
- [25] Pieter M.O. Gebraad, Paul A. Fleming, Jan-Willem van Wingerden, Comparison of actuation methods for wake control in wind plants, in: 2015 American Control Conference, ACC, IEEE, 2015, pp. 1695–1701.
- [26] Pieter M.O. Gebraad, F.W. Teeuwisse, J.W. Van Wingerden, Paul A. Fleming, S.D. Ruben, J.R. Marden, L.Y. Pao, Wind plant power optimization through yaw control using a parametric model for wake effects—a cfd simulation study, Wind Energy 19 (1) (2016) 95–114.

- [27] Miao Weipao, Li Chun, Yang Jun, Yang Yang, Xie Xiaoyun, Numerical investigation of wake control strategies for maximizing the power generation of wind farm, J. Solar Energy Eng. 138 (3) (2016) 034501.
- [28] Umberto Ciri, Mario A. Rotea, Stefano Leonardi, Effect of the turbine scale on yaw control, Wind Energy 21 (12) (2018) 1395–1405.
- [29] Umberto Ciri, Mario A. Rotea, Stefano Leonardi, Model-free control of wind farms: A comparative study between individual and coordinated extremum seeking, Renew. Energy 113 (2017) 1033–1045.
- [30] Ebrahim Mohammadi, Roohollah Fadaeinedjad, Gerry Moschopoulos, Implementation of internal model based control and individual pitch control to reduce fatigue loads and tower vibrations in wind turbines, J. Sound Vib. 421 (2018) 132–152.
- [31] Matthew A. Lackner, Mario A. Rotea, Passive structural control of offshore wind turbines, Wind Energy 14 (3) (2011) 373–388.
- [32] A. Staino, B. Basu, Dynamics and control of vibrations in wind turbines with variable rotor speed, Eng. Struct. 56 (2013) 58-67.
- [33] Steen Krenk, Martin Nymann Svendsen, J. Høgsberg, Resonant vibration control of three-bladed wind turbine rotors. AIAA J. 50 (1) (2012) 148–161.
- [34] Fiona Dunne, Lucy Y. Pao, Alan D. Wright, Bonnie Jonkman, Neil Kelley, Adding feedforward blade pitch control to standard feedback controllers for load mitigation in wind turbines. Mechatronics 21 (4) (2011) 682–690.
- [35] David J. Malcolm, A. Craig Hansen, Windpact Turbine Rotor Design Study: 2000– June 2002 (Revised), Technical Report, National Renewable Energy Lab.(NREL), Golden, CO (United States), 2006.
- [36] Emmanuvel Joseph Aju, Dhanush Bhamitipadi Suresh, Yaqing Jin, The influence of winglet pitching on the performance of a model wind turbine: Aerodynamic loads, rotating speed, and wake statistics, Energies 13 (19) (2020) 5199.
- [37] Dhanush Bhamitipadi Suresh, Emmanuvel Joseph Aju, Yaqing Jin, Turbulent boundary layer flow over two side-by-side wall-mounted cylinders: Wake characteristics and aerodynamic loads, Phys. Fluids 32 (11) (2020) 115104.
- [38] Pengyao Gong, Emmanuvel Joseph Aju, Yaqing Jin, On the aerodynamic loads and flow statistics of airfoil with deformable vortex generators, Phys. Fluids 34 (6) (2022) 067106.
- [39] Majid Bastankhah, Fernando Porté-Agel, A new miniature wind turbine for wind tunnel experiments. part i: Design and performance, Energies 10 (7) (2017) 908.
- [40] Devesh Kumar, Mario A. Rotea, Emmanuvel J. Aju, Yaqing Jin, Wind plant power maximization via extremum seeking yaw control: A wind tunnel experiment, Wind Energy 26 (3) (2023) 283–309.
- [41] Majid Bastankhah, Fernando Porté-Agel, A wind-tunnel investigation of wind-turbine wakes in yawed conditions, in: Journal of Physics: Conference Series, Vol. 625, IOP Publishing, 2015, 012014.
- [42] N. Tobin, H. Zhu, L.P. Chamorro, Spectral behaviour of the turbulence-driven power fluctuations of wind turbines, J. Turbul. 16 (9) (2015) 832–846.
- [43] Yaqing Jin, Sheng Ji, Leonardo P. Chamorro, Spectral energy cascade of body rotations and oscillations under turbulence, Phys. Rev. E 94 (6) (2016) 063105.
- [44] Huiwen Liu, Yaqing Jin, Nicolas Tobin, Leonardo P. Chamorro, Towards uncovering the structure of power fluctuations of wind farms, Phys. Rev. E 96 (6) (2017) 063117.
- [45] Y. Jin, S. Ji, L.P. Chamorro, Spectral energy cascade of body rotations and oscillations under turbulence, Phys. Rev. E 94 (6) (2016) 063105.
- [46] Theodore Von Karman, Progress in the statistical theory of turbulence, Proc. Natl. Acad. Sci. 34 (11) (1948) 530–539.
- [47] N. Tobin, A.M. Hamed, L.P. Chamorro, An experimental study on the effects ofwinglets on the wake and performance of a modelwind turbine, Energies 8 (10) (2015) 11955–11972.